ADVANCED MATERIALS TECHNOLOGIES
www.advmattechnol.de

ITO Top-Electrodes via Industrial-Scale PLD for Efficient Buffer-Layer-Free Semitransparent Perovskite Solar Cells

*Kassio P. S. Zanoni, Abhyuday Paliwal, M Angeles Hernández-Fenollosa, Pierre-Alexis Repecaud, Monica Morales-Masis, and Henk J. Bolink**

The deposition of transparent conductive oxides (TCO) usually employs harsh conditions that are frequently harmful to soft/organic underlayers. Herein, successful use of an industrial pulsed laser deposition (PLD) tool to directly deposit indium tin oxide (ITO) films on semitransparent vacuum-deposited perovskite solar cells without damage to the device stack is demonstrated. The morphological, electronic, and optical properties of the PLD deposited ITO films are optimized. A direct relation between the PLD chamber pressure and the solar cell performance is obtained. The semitransparent perovskite solar cells prepared exclusively by vacuum-assisted techniques had fill factors of 78% and exceeded 18% in power conversion efficiencies. This demonstrates that the direct deposition of TCO-based top electrodes without protective buffer layers is possible and leads to efficient devices.

1. Introduction

Almost all optoelectronic devices make use of transparent conductive oxides (TCO).[1–4] Sn-doped In_2O_3 (ITO) is the archetypal TCO in optoelectronics, yet there are many others, such as F-doped SnO_2 (FTO), Al-doped ZnO (AZO), Ga-doped ZnO (GZO), Zr-doped In_2O_3 (IZrO), to name a few. Examples of successful uses of TCO in optoelectronics are abundant, from well-established state-of-the-art devices such as silicon heterojunction solar cells and inorganic and organic light-emitting diodes (LEDs) to perovskite solar cells (PSCs), and organic solar cells.[5–8] There are also many examples of TCOs in new approaches that simultaneously require semitransparency and flexibility, such as semitransparent conductors, field-effect transistors, thermal shields, photo-detectors, and vertical transistors.[9–14] PSCs have attracted much interest since their onset in 2009 due to rapidly-increasing power conversion efficiencies (currently above 25% for small area cells). The perovskite layer and any adjacent charge transport layers can be fabricated in many ways using either solution-based processes or vacuum-assisted deposition. Vacuum-based deposition has the advantage of better control over the film thickness and is an additive method, moreover, it is a widely employed method of production of the before mentioned opto-electronic devices.[15,16]

Despite the benefits and promising perspectives of using TCOs in optoelectronics, the development of organic/TCO (TCO on top of organic) bi-layer structures is still a non-trivial challenge because of the generally harsh processing conditions involved in the deposition of the TCO layers.[17] For both lab- and industrial-scale deposition of TCO, magnetron sputtering is the most widespread technique. It is a vacuum-based process that employs direct current or radio frequency to excite a carrier gas (most commonly Ar) into a high kinetic energy plasma which bombards a target material, resulting in the transfer of fragments from the target to substrates positioned above it. However, the accelerated particles, together with side phenomena such as plasma luminescence and processing-induced heat, can easily damage soft organic semiconductor layers, leading to increased leakage current, as well as reduced efficiency and a lower lifetime of the optoelectronic device.[18,19] To overcome this limitation, a protective buffer layer is deposited prior to the TCO deposition.[17] Also, many efforts were proposed to minimize damages of sputtering deposition on buffer-layer-free stacks by lowering the power density threshold by changes in power, target to substrate distance, sputtering gas, and process pressure,[20–24] but at the expense of longer processing times.[22,25–29] Among these reports, the most efficient buffer-layer-free PSC using TCO top-electrode was achieved by Ramos et al. employing a post-annealed ITO sputtered directly onto a thick (290 nm) spiro-OMeTAD hole

K. P. S. Zanoni, A. Paliwal, H. J. Bolink
Instituto de Ciencia Molecular
Universidad de Valencia
C/Catedrático J. Beltrán 2, Paterna 46980, Spain
E-mail: henk.bolink@uv.es
M. A. Hernández-Fenollosa
Instituto de Tecnología de Materiales
Universitat Politècnica de Valencia
Camino de Vera s/n, Valencia 46022, Spain
P.-A. Repecaud, M. Morales-Masis
MESA+ Institute for Nanotechnology
University of Twente
Enschede 7500 AE, The Netherlands

The ORCID identification number(s) for the author(s) of this article can be found under https://doi.org/10.1002/admt.202101747.

DOI: 10.1002/admt.202101747

transport layer (HTL), however not exceeding 15.7% power conversion efficiency (PCE).[26] Later, Dewi et al. achieved PSCs with a higher PCE (17.7%) also employing low-power-sputtered ITO top-electrodes onto a thick spiro-OMeTAD layer, however, their best operating PSCs required a thin thermally evaporated Ag film as a protective layer to diminish damages on the HTL underlayer.[28] Therefore, there is a need for the development of new "soft" deposition techniques that can potentially allow smooth damage-free deposition of TCO top-electrodes, preferably without the need of post-annealing treatments.

Pulsed laser deposition (PLD) is another well-known vacuum-based technique for the deposition of TCOs.[30] PLD employs high-power laser pulses to vaporize the surface of a target material leading to the formation of a plasma and allows for a wider range of deposition pressures, usually much larger than those used for sputtering deposition.[31] With increasing the chamber pressure, the background gas inside the chamber decreases the kinetic energy of the ablated species in the plasma via thermalization, hence the impact of the deposition on the substrate is expected to be less damaging.[17] Despite its encouraging perspectives, there are just a few reports on the successful usage of PLD-deposited TCOs on thin-film photovoltaic devices, such as AZO, GZO, and B-doped ZnO bottom-contacts for a Cu(In,Ga)Se_2 thin-film solar cell,[32] and AZO or GZO top-electrodes for organic solar cells,[3,33] as well as IZrO and ITO as the top-electrode on PSCs,[2,34] and perovskite-based tandem solar cells.[35] However, in these perovskite device examples, the PCE did not exceed 15%. Apart from TCO top-electrodes, PLD has also been employed for the deposition of oxide charge transport layers, such as ZnO on organic solar cells[36] and PSCs,[37] as well as NiO in PSCs.[38]

Here we report on the effect of the deposition chamber pressure on the optical and electronic properties of ITO (2:98 wt% SnO_2:In_2O_3) using an industrial PLD tool and its effect to achieve high efficiency buffer-layer-free semitransparent perovskite solar cells. We employ optimized deposition parameters operating at room temperature to obtain ITO layers with absorptance values below 10% throughout the visible wavelength range with a low sheet resistance of 25 Ω $\square^{-1}$ (for 160 nm thick films). This process was furthermore used to deposit >100 nm of ITO directly on top of a device stack consisting of 500 nm of perovskite covered by organic semiconductor layers with a total thickness below 32 nm, hence without any protective layer. Using this method of direct PLD deposited ITO we achieve thin film semi-transparent perovskite solar cells with power conversion efficiencies exceeding 18% PCE.

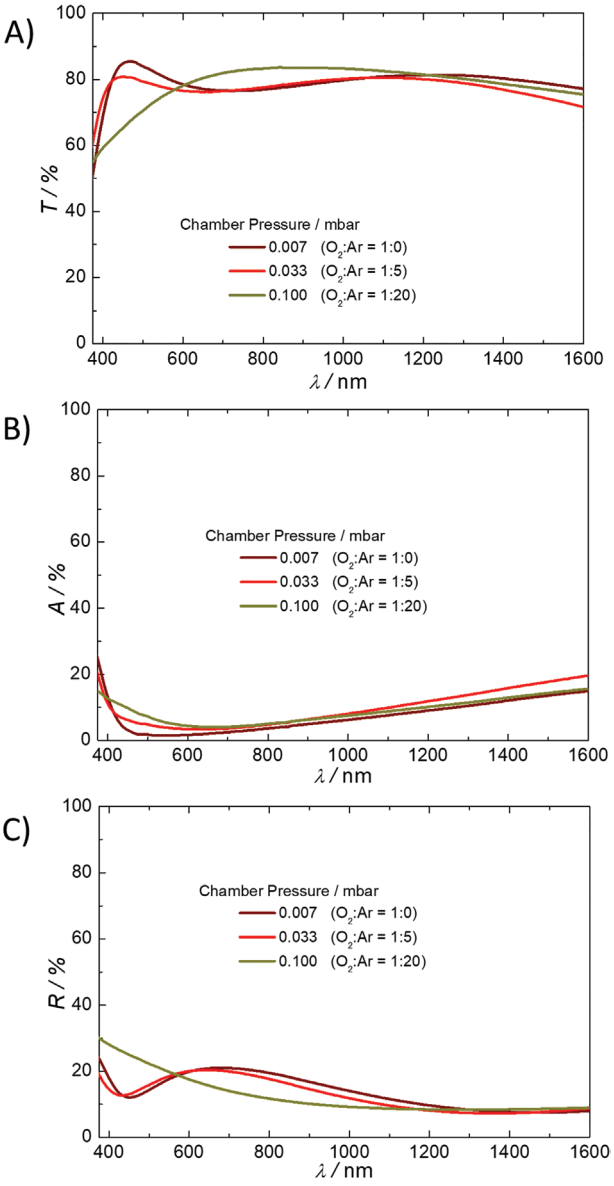

Figure 1. A) Transmittance, B) absorptance, and C) reflectance spectra of ITO films deposited under different pulsed laser deposition (PLD) chamber pressures.

2. Results and Discussion

2.1. ITO Film Characterization

The ITO deposition conditions were optimized using a chamber pressure in the range of 0.007 to 0.100 mbar, controlled by a constant injection of an oxygen/argon gas mix, and the laser fluence was kept at a constant value of 1.5–1.6 J cm^{-2} for all investigated pressures. As the chamber pressure increases the plasma shape expands (Figure S1A, Supporting Information). This decreases the amount of material deposited per area leading to twofold decrease in the total growth (nm per cycle) as the chamber pressure increases from 7×10^{-3} to 1×10^{-1} mbar (Figure S1B, Supporting Information). The morphology of the films is also affected (Figure S1C Supporting Information) by the chamber pressure, leading to the deposition of a flat, pinhole-free film at 10^{-3} mbar, and films with gradually increasing porosity and granular structures for increasing pressures.[39] The growth rate when using a laser frequency of 25 Hz for the lower pressure process is 120 nm h^{-1}. The X-ray diffraction pattern of the as-deposited ITO films deposited at any of the investigated PLD chamber pressures reveals that the films are of amorphous nature, (Figure S2, Supporting Information), similarly to previous reports.[40–43] The pristine PLD deposited TCO layers can be annealed causing the amorphous films to become polycrystalline;[42,43] however, our aim is to verify if PLD

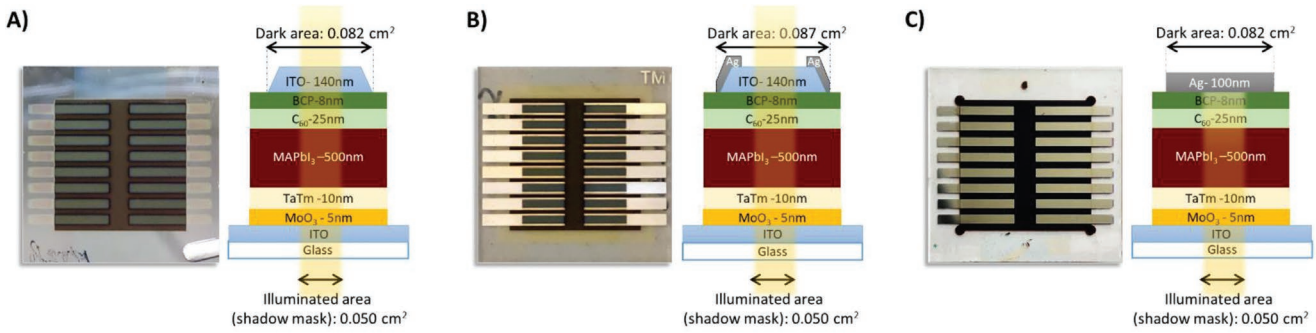

Figure 2. Top view photographs and cross-section device structures (not in scale) of semitransparent devices using 140 nm of pulsed laser deposition (PLD)-deposited ITO top-electrodes, without A) or with Ag grids B), and of a standard device using 100 nm of Ag top-electrode C).

can be used to deposit ITO on top of perovskite and organic semiconductors and therefore, no annealing step was performed to the as-deposited ITO layer.

The transmittance, reflectance, and absorptance spectra of the ITO films on glass substrates are shown in **Figure 1**A–C. The main difference in the transmittance and reflectance spectra for the ITO films deposited at 0.1 mbar, as compared to the other pressures, is related to the lower thickness of the films, which occurs due to the higher deposition pressure (when keeping equal deposition time or the number of pulses). Overall, the films present absorptance below 10% in the visible range, until 1200 nm. Increased parasitic absorption occurs in the NIR as the near-infrared radiation interacts with the free electrons in the conduction band,[44] leading to increased absorptance hence decreased transmittance at wavelengths higher than 1150 nm. Some interference phenomena can also occur in the visible region depending on the thickness of the film (Figure S3, Supporting Information). In addition to thickness, slight differences in transmittance, reflectance, and absorptance can be related to the O_2:Ar ratio during deposition (Figures S4 and S5A, Supporting Information). Similar trends in transmission spectra of PLD-deposited ITO films as a function of chamber pressure and thickness were observed by Kim et al. for ITO films deposited at 300 °C[44] and by Smirnov et al. for PLD ITO deposited at room temperature.[34]

As expected, the sheet resistance increases for the less-dense films deposited at higher chamber pressures (Figures S4 and S5, supporting information). In fact, a surprisingly linear correlation is observed between the PLD chamber pressure and the logarithmic of the sheet resistance and conductivity (Figure S5B–D, Supporting Information). The fit of the linear relation leads to an R-squared (coefficient of determination calculated from the simple linear regression) higher than 0.94. A resistivity as low as 4×10^{-4} Ω cm is reached for samples deposited at 7×10^{-3} mbar, similar to previous publications on PLD grown ITO on glass at room temperature, using either UV-excimer or 355-Nd:YAG lasers.[40–42,44–47]

2.2. Use of ITO Top-Electrodes on PSCs

To verify the impact of the PLD deposited ITO films on organic and perovskite-based semiconducting films, they were deposited on top of the following stack of layers:

glass/ITO (160 nm)/MoO_3 (6 nm)/TaTm (10 nm)/$MAPbI_3$ (500 nm)/C_{60} (25 nm)/BCP (7 nm) (where TaTm is N4,N4,N4″,N4″-tetra([1,1′-biphenyl]-4-yl)-[1,1′:4′,1″-terphenyl]-4,4″-diamine, C_{60} is fullerene, and BCP is bathocuproine). This sequence of layers has been used to prepare efficient thin film opaque p-i-n solar cells using a Ag metal top electrode (it is referred to as p-i-n because the positive charge carriers are extracted at the electrode of light incidence and the negative charge carriers to the counter electrode).[16] We have used this exact same stack to verify if we can directly deposit ITO by PLD. For the ITO PLD deposition, the substrates were aligned to shadow masks to obtain the electrode layout indicated in **Figure 2**A, with 16 rectangular pixels of 0.082 cm^2, eight on each side of the substrate, allowing for significant statistics. To ensure maximum current collection and minimize resistance losses, we also evaluated the use of thin (100 nm) silver grid lines (thermally-evaporated) surrounding the PLD-ITO contacts, as demonstrated in Figure 2B. The addition of the silver grid lines leads to a slightly larger electrode overlap area of 0.087 cm^2. For comparison, standard non-transparent electrode reference devices were also fabricated using a reflective silver (Ag) layer (100 nm) as the top-electrode (Figure 2C), which leads to an electrode overlap area of 0.082 cm^2. Although the semitransparent and reference devices have slightly different electrode overlap areas, all the samples were irradiated from the glass side using an illumination mask positioned at the center of the pixels with an opening of 0.050 cm^2 and as such defining the active area to this value for all pixel variations.

The cross-sectional structure of the constructed stacks was investigated using a scanning electron microscope, in which some $MAPbI_3$ crystals are observable in **Figure 3**A. Figure 3B shows a top view SEM image of the PLD-ITO top-electrode. It can be seen that the ITO layer is not perfectly flat but rather shows some microfeatures evidencing that ITO films deposited by PLD conformally follows the small thickness variations of the underlying stack.[48]

To verify that the ITO deposition does not lead to damage in the device stack, electrical and optical analysis were also performed on the semi-transparent device stacks. These were compared with the results from opaque reference devices that contain a thermally sublimed Ag metal top electrode. For this evaluation we deposited ITO on the device stacks using a range of different PLD chamber pressures, going from 0.007 to 0.1 mbar. The dark current density versus voltage (J–V) for devices

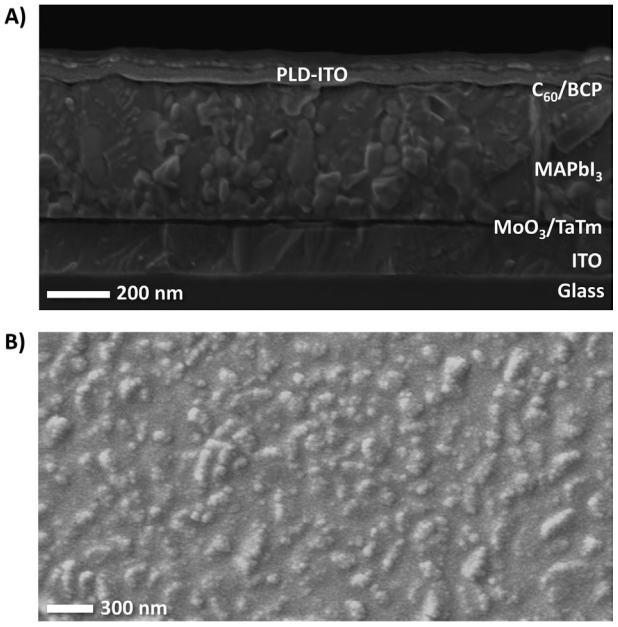

Figure 3. A) Cross section and B) topview scanning electron microscope (SEM) images of a semitransparent device using ITO top-electrode deposited by pulsed laser deposition (PLD) at 0.033 mbar.

containing PLD ITO deposited at 0.007, 0.033, and 0.1 mbar (i.e., with 28, 80, and 840 Ω □$^{-1}$, respectively) are shown in **Figure 4**A. The global trend of the dark current density for the semitransparent devices is similar to that of the reference device that has a reflecting Ag back electrode. We note that due to scan direction and scan rate the minimum current density is not at zero volts, but this is an artifact of the analysis. When taking the second scan the minimum does coincide with zero volts as shown in Figure S6, Supporting Information. The current density around zero volt, resembling the leakage current, is slightly higher for the device for which the PLD-ITO was deposited at the lowest pressure, and in some cases (device with PLD-ITO deposited at a chamber pressure of 0.033 mbar) the leakage current is lower than for the reference device. The current density around 1 volt is virtually the same for all devices. This implies that there are no direct shorts generated by the direct deposition of the PLD-ITO on this stack. It is known that intrinsic $MAPbI_3$ has a rather low conductivity and therefore, the combined stack of organic and perovskite semiconducting layers amounts to some 550 nm. Therefore, it is possible that some ITO did penetrate the top organic layers but this does not lead to an increase in current density due to the highly resistive (in the dark) perovskite film. We, therefore, also evaluated a stack without the perovskite film, and also in this

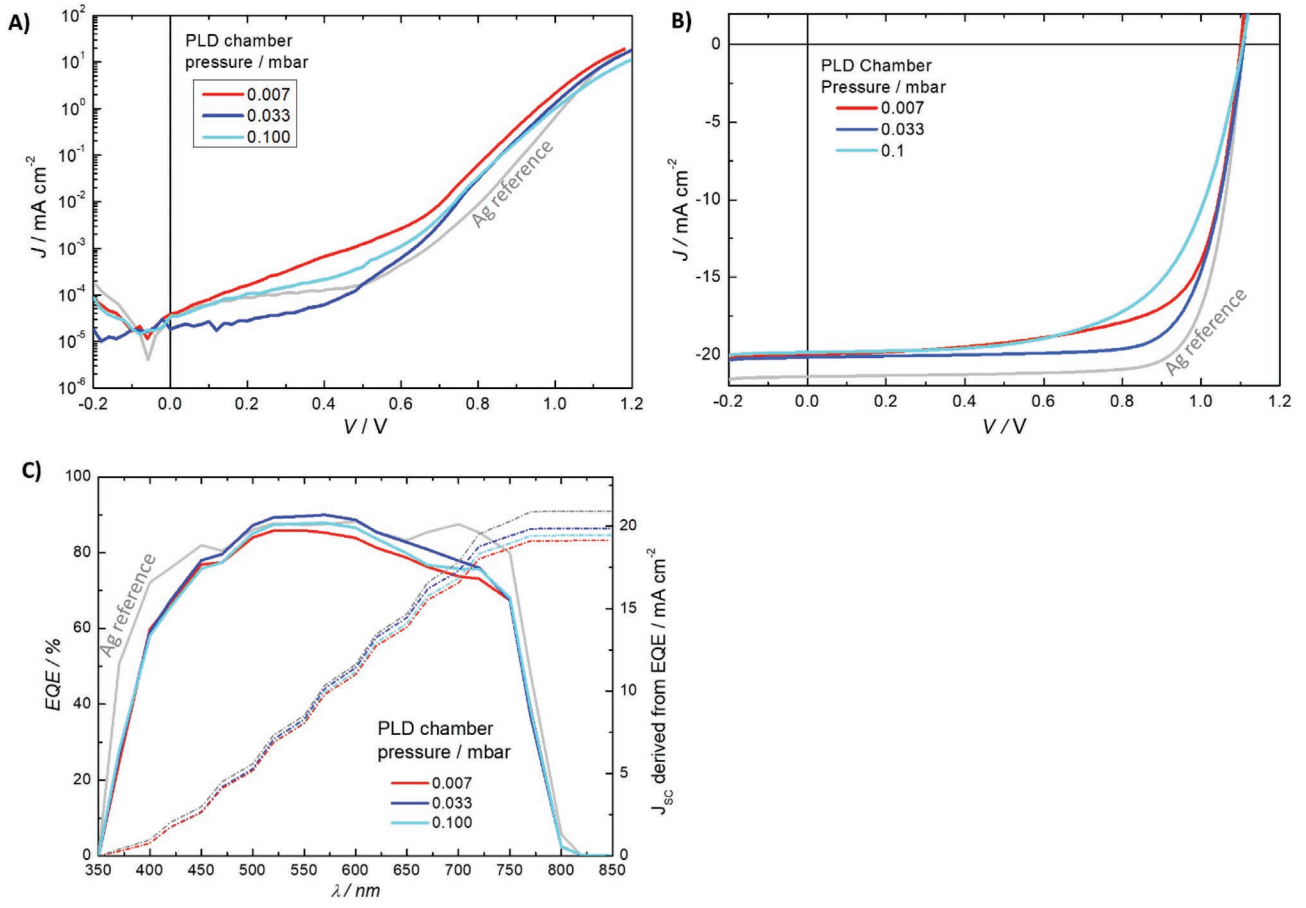

Figure 4. A) Dark *J*–*V* curve, B) illuminated *J*–*V* curves (measured under AM 1.5 G irradiation at 100 mW cm^{-2} at room temperature), C) External quantum efficiency (EQE) spectra and integrated J_{SC} derived from the EQE spectra for devices with ITO top-electrodes deposited under different pulsed laser deposition (PLD) chamber pressures.

case no significant increase in the leakage current was observed (Figure S7, supporting information).

Another, way to assess if the ITO layer is in contact with the perovskite layer is to evaluate the solar cells under illumination. The current density versus voltage under 1 sun illumination for three representative devices is depicted in Figure 4B (only the forward scan is shown, the forward and reverse scan are identical as shown in Figure S8, Supporting Information). For these three devices, the open-circuit voltage (V_{oc}) is exactly the same. This is a strong indication that the ITO is not in direct contact with the perovskite as this would introduce some recombination losses at the perovskite-ITO interface, corroborating the conclusions drawn from the SEM cross-section, and the dark *J*–*V* curves in that the ITO is conformally coated on top of the organic semiconducting layers. The main difference in the *J* versus *V* curves obtained under 1 sun illumination is the reduced short circuit current density (J_{SC}) of the semi-transparent devices compared to the reference devices. This difference is due to the lack of reflective back contact and therefore the effective pathlength of the sunlight in the ITO-containing devices is reduced which leads to a loss in the generated current. Another factor that is different for the semitransparent cells is the fill factor (FF) which is slightly lower for the devices that use ITO from the lowest and highest chamber pressures. There is a clear effect of the gridlines on the devices that were finished with a top ITO electrode deposited using a chamber pressure in the range of 0.022–0.047 mbar which has virtually the same FF as the reference device. Devices that do not have the gridlines do suffer from a lower FF, as will be addressed in the following paragraphs. The external quantum efficiency (EQE, Figure 4C) of the PLD-ITO-based semitransparent devices is slightly lower than the reference device, in particular at the band edge where the optical path length has the highest impact.

Although the samples without Ag grids show a slightly lower J_{SC} than the samples having the grids, the difference is statistically insignificant. As expected for devices in short circuit conditions, the EQE (Figure 4C) and J_{SC} (**Figure 5**A) are independent of the ITO-deposition pressure, with values around 19–20 mA cm^{-2}, except for the 0.100 mbar sample without the grids, which shows a significantly lower J_{SC} mainly because the

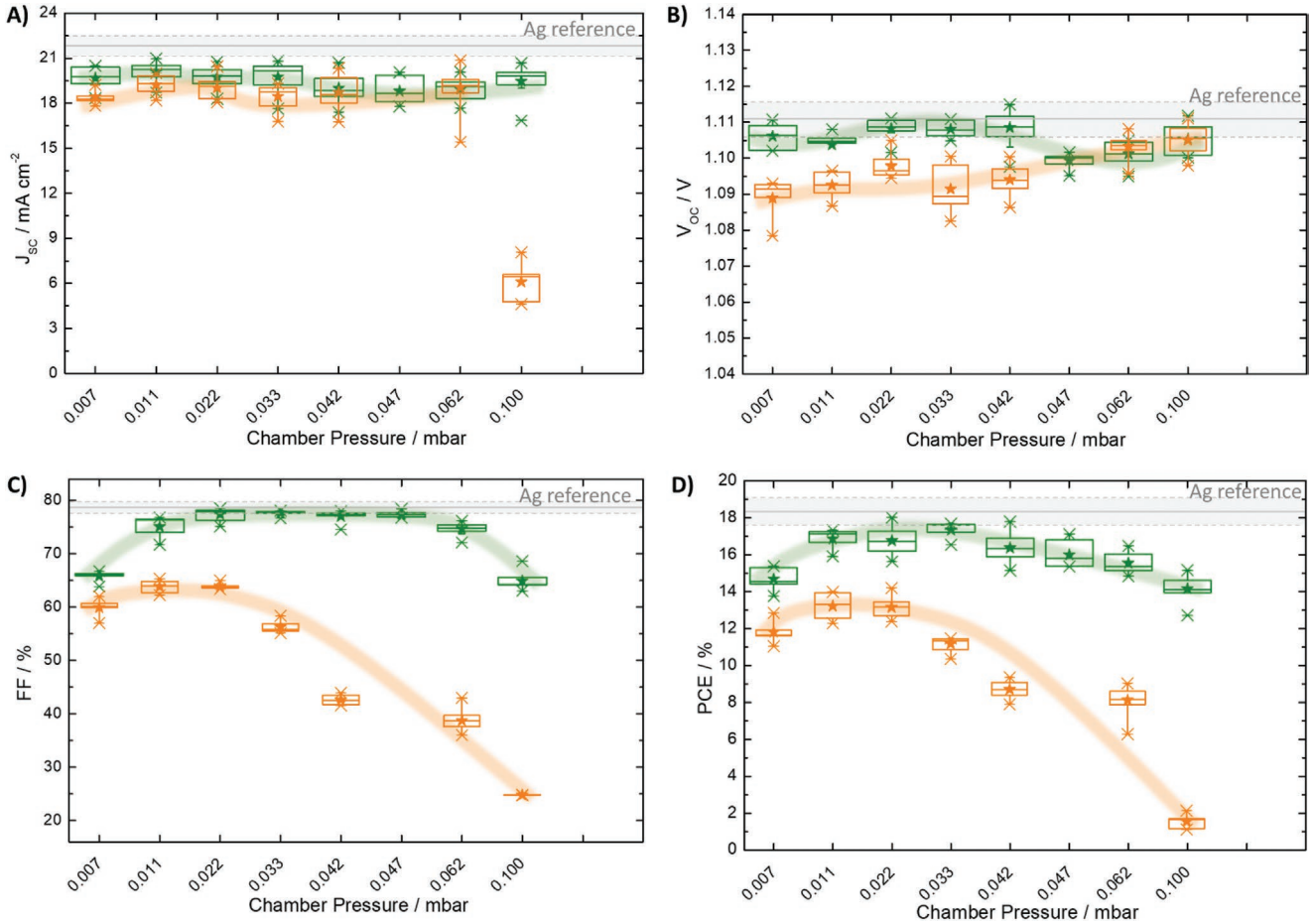

Figure 5. Statistic distribution of the photovoltaic performance of ITO/MoO_3/TaTm/$MAPbI_3$/C_{60}/BCP/top contact devices, with ITO top-electrodes deposited under different pulsed laser deposition (PLD) chamber pressures. A) J_{SC}, B) V_{OC}, C) FF, and D) PCE versus PLD chamber pressure of illuminated devices with (green) or without (orange) Ag grid. At each chamber pressure, the ideal O_2 partial pressure was set following the linear fit found in Figure S5A, Supporting Information. Sample size: at least eight samples for each pressure. Symbol interpretation: × at the bottom of the rectangular box stands for minimum value within the samples; bottom of the rectangular box stands for 25% of the samples; horizontal line in the middle of the rectangular box stands for 50% of the samples; top of the rectangular box stands for 75% of the samples; × at the top of the rectangular box stands for maximum value within the samples; star stands for mean.

ITO obtained at this pressure is deposited too softly and has less adhesion to the glass, which can be easily scratched away by the alligator clips during measurement; nevertheless, the use of Ag grids reestablishes a proper contact.

The V_{OC} (Figure 5B) of samples without Ag grid ranges from an average value of 1.09–1.10 V for the devices that have an ITO top electrode deposited at a chamber pressure between 0.007 and 0.1 mbar. The V_{OC} for the devices with gridlines is slightly higher and reaches 1.12 V almost similar over the range of devices. Therefore, the V_{OC} in the Ag-grid containing devices is very close in magnitude to the reference device with the reflective Ag top electrode.

The series resistances of the investigated devices were derived from their illuminated *J–V* curve by calculating the inverse of the slope near the open circuit.[49] For the cells without the Ag grids, the lowest series resistance is 13.1 mΩ cm^{-2} derived for the device finished with a top ITO electrode deposited using a chamber pressure of 0.007 mbar, which increases to 17.4 mΩ cm^{-2} for devices having ITO deposited at 0.033 mbar, and finally increasing further to 67.2 mΩ cm^{-2} for devices with ITO fabricated at 0.100 mbar. Therefore, this trend is very similar to the one observed for the ITO's sheet resistance versus PLD chamber pressure. In fact, the logarithmic of the series resistance derived from the illuminated *J–V* curve of non-grided devices also follows a linear correlation to the PLD chamber pressure, in a very similar fashion to the linear correlation observed in Figure S5, Supporting Information for the ITO's sheet resistance. On the other hand, the lowest series resistance derived from the *J–V* curves for cells that contain a small Ag grid is 3.9 mΩ cm^{-2} for the ITO deposited at 0.007 mbar, just slightly increasing to 4.8 mΩ cm^{-2} for 0.033 mbar, then slightly increasing again to only 6.9 mΩ cm^{-2} for 0.100 mbar. These results prove that the employed metal grids act effectively diminishing the series resistances of the devices, as expected.

The series resistance for cells without grids leads to variations in the FF, as shown in Figure 5C. For these cells, the tendency of the FF is in line with the increasing ITO sheet resistance and device series resistances. To verify this correlation between FF and the obtained series resistances, we calculated the predicted FF using approximations for a device under the large influence of series resistance (by means of Equation (21) in reference[50] – note that this equation considers only the influence of series resistance, but with negligible shunt resistance, which makes the calculations more practical, yet it can lead to small deviations). As exhibited in Figure S9A, Supporting Information-Supporting Information, the trend observed for the calculated FF is in very good agreement to the one for the experimentally observed FF, revealing that the lower FF for devices with ITO top contacts fabricated at higher pressures is indeed caused by their higher series resistances.

On the other hand, the cells with Ag grids, have a lower dependence of the FF on the ITO series resistance, reaching values as high as 77%–79%, which is similar to that of the Ag reference devices. The predicted FF (calculated from their series resistance) of these Ag-grided devices are also in very good agreement to their experimentally observed FF, as exhibited in Figure S9B, Supporting Information. Therefore, the improved FF of Ag-grided samples (as in comparison to non-grided) is in accordance with the diminished series resistances observed when the metal grids are implemented.

The devices in which the ITO layer was deposited at a chamber pressure of 0.007 mbar has a rather low FF, lower than what is expected from the ITO's sheet resistance (28 Ω □$^{-1}$) or the device's series resistance (13.1 mΩ cm^{-2} for non-grided and 3.9 mΩ cm^{-2} for Ag-grided), pointing to other factors affecting the total resistance across the device. In fact, the shape of its *J–V* curve – in particular the slope near short-circuit until more or less the voltage of maximum power point – is typical of a device limited by shunt resistances,[49] which could indicate partial penetration of the ITO in the organic semiconductor films. This does not happen when the ITO is deposited at higher deposition pressures. To check if indeed this might be the case, we reduced the BCP thickness away from the optimum 7 nm in devices that employ an ITO layer that is deposited at 0.033 mbar (Figure S10, Supporting Information) and compare the device performance with that of the anomalous one. The V_{OC} and FF for the devices with a BCP layer of 3 nm matches the performance of the anomalous one in which the ITO was deposited at a chamber pressure of 0.007 mbar. Hence, it is likely that the PLD-ITO top-electrode deposited at lower chamber pressures might penetrate a few nm in the BCP layer. This would lead to less blocking behavior and cause a loss in FF. Moreover, sample zero in Figure S10, Supporting Information (with only C_{60} in the electron transport layer) exhibits a much lower V_{OC} (0.75 V) than devices with C_{60}/BCP heterojunction (1.11 V), indicating that ITO did not completely penetrate across BCP in the 0.007 mbar device.

Ultimately, because the samples all show J_{SC} or V_{OC} with very similar magnitudes among each other, their PCE is affected primarily by their FF, for which the trends versus chamber pressure in Figure 5D are almost the same as the ones in Figure 5C. The devices that employ PLD ITO deposited with a chamber pressure ranging from 0.022 to 0.033 mbar that also have an Ag grid have very little spread in performance and have PCEs of around 17.5% on average. These results are remarkably similar to the Ag cathode reference (average PCE = 18.3%), only slightly lower due to the lower EQE/J_{SC} of the semitransparent samples. From these experiments, we therefore conclude that no additional damage is occurring when depositing PLD-ITO instead of Ag. To try and verify that indeed no ITO is reaching the perovskite interface, we performed two additional analyses. In the first, we employed X-ray photoelectron spectroscopy (XPS) on delaminated devices. For this trial, we peeled the top layers off by following the procedure described by de Bastiani et al.,[51] in which a polyimide tape is employed as a peeling agent, and then XPS was obtained on the surfaces of both the peeled device and the peeled off films that stick to the tape (Figure S11, Supporting Information, summarizes the peeling procedure). As summarized in Table S1, Supporting Information, the surface of the peeled device consists mainly of C and N, with a very low Pb and In content (0.01 and 0.04%, respectively). The peeled-off films, on the other hand, contain C, N, In, and Sn and no detectable Pb. These results indicate that we delaminated the device in the middle of the ETL with $MAPbI_3$/C_{60} on one side and C_{60}/BCP/PLD-ITO on the other, as similarly observed by de Bastiani et al.[51] It is important to note that the derisory Pb and In observed on the peeled device most likely come from the rudimentary procedure of peeling with a tape, that in some very small areas might either a) peel off too much C_{60} and expose $MAPbI_3$ or b) leave some traces of ETL/ITO unpeeled.[51] This

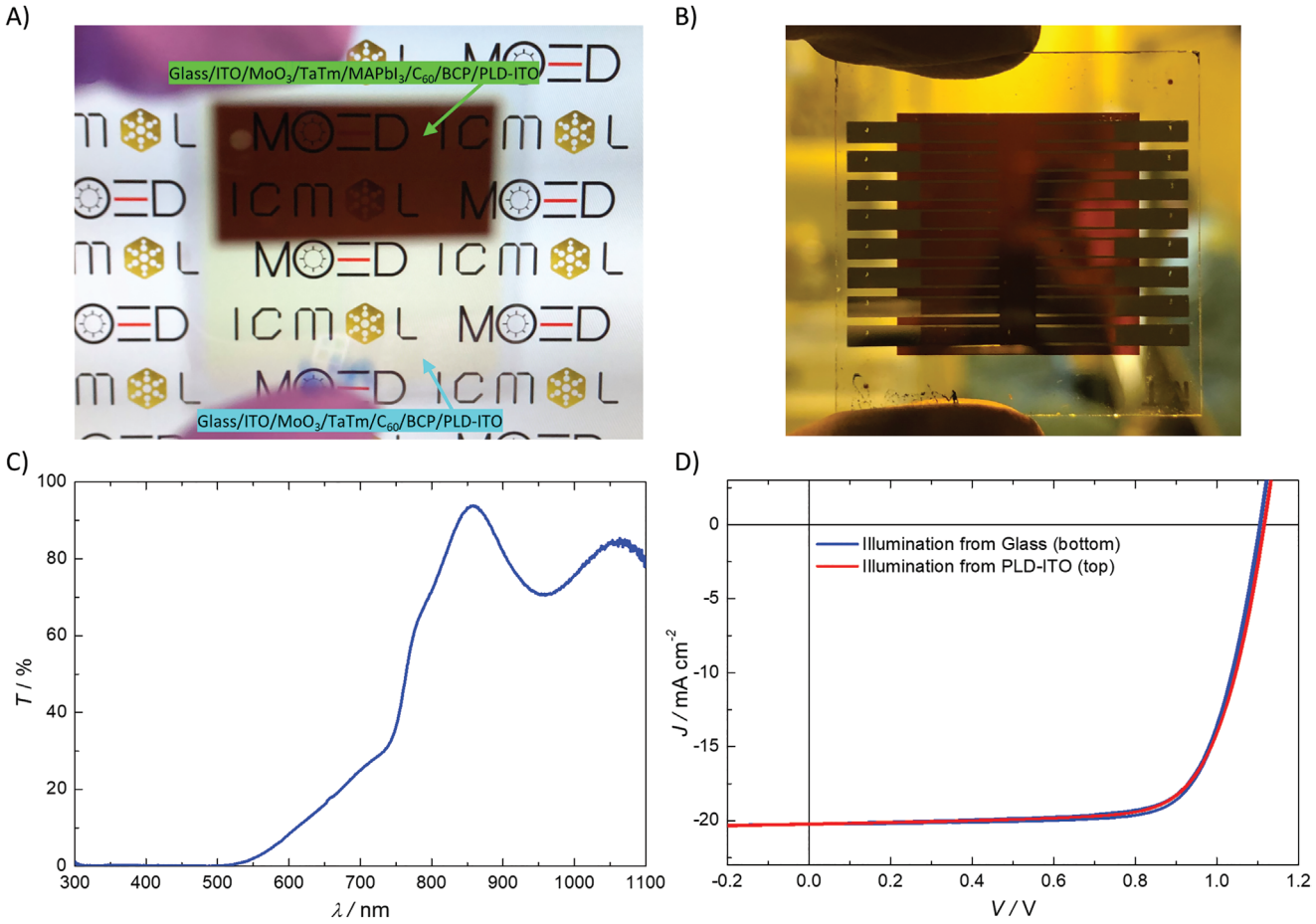

Figure 6. A) A picture of a squared substrate – half coated with a full ITO/MoO_3/TaTm/$MAPbI_3$/C_{60}/BCP/PLD-ITO(0.033 mbar) PSC stack and the other half coated with a ITO/MoO_3/TaTm/C_{60}/BCP/PLD-ITO(0.033 mbar) diode stack (without $MAPbI_3$) – held in front of the logos of our institute and of our research group. B) A picture of a PSC with ITO top contacts pulsed laser deposition (PLD)-deposited at 0.033 mbar and Ag grids held vertically in the air, with a colleague working in the laboratory at the background. C) Transmittance spectrum of the full semitransparent PSC stack. D) *J–V* curves of PSCs with ITO top contacts PLD-deposited at 0.033 mbar (with Ag grids) illuminated either from the glass side (bottom illumination) or from the PLD-ITO side (top illumination); measured under AM 1.5 G irradiation at 100 mW cm^{-2} at room temperature.

data shows that very little In is found in the part of the C_{60} layer still on top of the $MAPbI_3$ layer and hence that the penetration depth of the ITO using this PLD process is less than 20 nm. In a second approach, we used energy-dispersive X-ray (EDS) mapping on a crosssection of the device, focussing on the $MAPbI_3$/C_{60}/BCP/PLD-ITO interfaces. As shown in Figure S12, Supporting Information, a high count of Pb and C (from MA^+) is observed in the $MAPbI_3$ layer. The Pb content starts to decline when reaching the C_{60}/BCP interface. As we use dry deposition methods no Pb is mixed with the C_{60}/BCP layer (as corroborated from the XPS data). Hence, the detection of Pb in the C_{60}/BCP layer is an artifact of this analytical method as EDS is a low resolution method.[52] More importantly, the counts of the elements of ITO, In, Sn, and O, are zero through the perovskite layer and only start to increase at the ITO interface with C_{60}/BCP. The carbon signal increases when we scan the ETL layer, as expected as there the presence of Carbon is higher.

Hence, juding from the good device performance, the XPS data for the delaminated devices, and the EDS on the cross-section, we conclude that no ITO reaches the perovskite/ETL interface.

Highlighting the semitransparency of our devices, **Figure 6**A,B show some pictures of the full ITO/MoO_3/TaTm/$MAPbI_3$/C_{60}/BCP/PLD-ITO(0.033 mbar) stack and Figure 6C exhibits its transmittance. These semitransparent PSCs with PLD-ITO deposited at 0.033 mbar were tested under illumination from both sides, either from the glass or from the PLD-ITO top contact (device samples were encapsulated by 30 nm of Al_2O_3 deposited by atomic layer deposition, as described in our previous publication).[53] As shown in Figure 6D, both *J–V* curves are very similar. Our ongoing investigation is on elucidating the differences between top and bottom illumination of both p-i-n and n-i-p configurations.

3. Conclusion

Using an industrial PLD tool we have evaluated the dependence of the optical and electronic properties of ITO (2:98 wt% SnO_2:In_2O_3) on the deposition chamber pressure. With optimized deposition parameters operating at room temperature,

ITO layers with absorptance values below 10% in the visible wavelength range and low sheet resistance of 25 $\Omega\ \square^{-1}$ are obtained. This process was used to deposit ITO directly on top of a photovoltaic device stack consisting of 500 nm of $MAPbI_3$ perovskite covered by organic semiconductors with a thickness ≈30 nm, hence without any protective layer. Using this method of direct PLD deposited ITO we achieve thin film semi-transparent perovskite solar cells with power conversion efficiencies exceeding 18%.

4. Experimental Section

N4,N4,N4″,N4″-tetra([1,1′-biphenyl]-4-yl)-[1,1′:4′,1″-terphenyl]-4,4″-diamine (TaTm) was provided by Novaled GmbH. Fullerene (C_{60}) was purchased from Sigma–Aldrich. PbI_2 was purchased from Tokyo Chemical Industry CO. MoO_3, CH_3NH_3I (MAI), and bathocuproine (BCP) were purchased from Lumtec.

Pre-patterned ITO coated glass substrates were purchased from Naranjo Substrates. They were cleaned by subsequent immersions in soap, water, deionized water, and isopropanol in a sonication bath for 5 min each, followed by insertion in an ozone chamber with UV irradiation for 20 min.

Industrial Scale PLD System: The ITO films were deposited on glass substrates or directly on the toplayers of PSCs at room temperature using a Solmates large area PLD 200 mm system in the University of Valencia facilities. The system is equipped with a droplet trap to reduce the number of undesired particles on the deposited film, which allows for a homogeneous deposition on large areas >615 cm^2, with less than 1.5% variation in TCO thickness and sheet resistance. This PLD tool is coupled to a N_2 glovebox, to minimize any detrimental effects from O_2 and moisture on the performance of the finally produced devices. A Lightmachinery's IPEX-700 KrF excimer laser (λ = 248 nm) was employed, setting the repetition rate at 25 Hz and a fluence of 1.5–1.6 J cm^{-2}. The source material for ITO deposition was a SnO_2:In_2O_3 ceramic target with 2:98 wt.%, acquired from Pi-kem. The substrates were taped to shadow masks to obtain the final deposition layouts.

Device Fabrication: All the solar cell layers were prepared in the University of Valencia facilities by thermal vacuum deposition performed in vacuum chambers evacuated to a pressure of 10^{-6} mbar, which were integrated into a nitrogen-filled glovebox (H_2O and O_2 < 0.1 ppm). In general, the vacuum chambers were equipped with temperature-controlled evaporation sources (Creaphys) fitted with ceramic crucibles. The sources were directed upward with an angle of ≈90° with respect to the bottom of the evaporator. The distance between the substrate holder and the evaporation source was approximately 20 cm. Individual quartz crystal microbalance (QCM) sensors monitored the deposition rate of each evaporation source and another one close to the substrate holder monitored the total deposition rate.

For the perovskite deposition, MAI and PbI_2 were co-evaporated at the same time by measuring the deposition rate of each material in two different sensors (with rates of 0.45 and 0.50 Å s^{-1}, respectively) and obtaining the total perovskite thickness in a third one located closer to the substrates (rate around 0.7 Å s^{-1}), leading to a 500 nm thick perovskite. TaTm, $C_{60,}$ and BCP were sublimed in the same vacuum chamber with temperatures around 300, 420, and 140 °C, respectively, and the precise evaporation rate and deposited film thickness were controlled by the QCM sensors. In general, the deposition rate for TaTm and C_{60} was 0.6 Å s^{-1} while the thinner BCP layer was evaporated around 0.4 Å s^{-1}. MoO_3 and Ag were evaporated in another vacuum chamber using aluminum boats as sources by applying currents ranging from 2.0 to 4.5 A.

The devices were encapsulated using atomic layer deposition of Al_2O_3 at 40 °C, using a protocol recently published by us.[53]

General Characterization: Absorption spectra were collected using a fiber optics-based Avantes Avaspec2048 spectrometer. X-ray photoelectron spectra of sample surfaces were recorded using a Thermo Scientific *K*-Alpha with a monochromatic Al Kα X-ray source (1486.6 eV) available in the ICMol facilities; data were analyzed and deconvoluted with Avantage software; the binding energies were adjusted to the standard C 1s peak at 284.6 eV. SEM images and EDS mapping were recorded using a ZEISS AURIGA Compact field emission scanning electron microscope with focused ion beam (FIB). A FIB is comparable to an SEM, yet instead of electrons, it uses a beam of Ga^+ ions, which are 130 000 times heavier than electrons; consequently, the interaction with the specimen is significantly stronger, whereas the penetration level is lower. Thus, ions produce a break of the chemical bonds and ionization of the substrate atoms. Since the ion beam can be focused and monitored, this effect can be used to modify the structure of the specimen on a nanometric scale. Thicknesses were measured with an Ambios XP1 mechanical profilometer. X-ray diffraction was measured with a Panalytical Empyrean diffractometer equipped with CuKα anode operated at 45 kV and 30 mA and a Pixel 1D detector in scanning line mode; single scans were acquired in the 2 θ = 5–50° range in Bragg–Brentano geometry in air. Hall effect measurements were obtained using an Ecopia HMS-3000 Hall Measurement System.

The EQE was estimated using the cell response at a different wavelength (measured with a white light halogen lamp in combination with band-pass filters). We determined the spectral mismatch factor (M) using a calibrated Silicon reference cell (supplied by ECN, from the Netherlands) via the correction methodology published by NREL and found M to be very close to 1 (0.9937) as expected for the AAA solar simulator used.[54] The *J–V* curves for the solar cells were recorded using a Keithley 2612A SourceMeter in a −0.2 and 1.2 V voltage range, with 0.01 V steps and integrating the signal for 20 ms after a 10 ms delay, corresponding to a speed of about 0.3 V s^{-1}. The devices were illuminated under a Wavelabs Sinus 70 AAA LED solar simulator. The light intensity was calibrated before every measurement using a calibrated Si reference diode equipped with an infrared cutoff filter (KG-3, Schott). For all devices, we compare the calculated J_{sc} from the EQE with that obtained from the *J–V* analysis of the cells illuminated with the AAA Led solar simulator. During the experiment, the encapsulated devices were exposed to air; the temperature was stabilized at 298 K during the entire measurement using a cooling system controlled by a Peltier element.

Statistical Analysis: For the statistics presented in Figure 5, the minimum sample size was eight samples for each condition described. The statistical distribution was treated using the software Origin 2021.

Supporting Information

Supporting Information is available from the Wiley Online Library or from the author.

Acknowledgements

The research leading to these results has received funding from the European Research Council (ERC) under the European Union's Horizon 2020 Research and Innovation Programme (Grant agreement No. 834431). The authors acknowledged support from the Comunitat Valenciana (IDIFEDER/2018/061 and PROMETEU/2020/077), as well as by the Ministry of Science and Innovation (MCIN), and the Spanish State Research Agency (AEI): Project PCI2019-111829-2 funded by MCIN/AEI/10.13039/501100011033 and by the European Union; Project CEX2019-000919-M funded by MCIN/AEI/10.13039/501100011033, and the King Abdullah University of Science and Technology (KAUST) Office of Sponsored Research (OSR-2019-CRG8-4093.2). K.P.S.Z. acknowledged funding from Comunitat Valenciana (APOSTD/2021/368). AP acknowledged his Grisolia grant from the Comunitat Valenciana (GRISOLIAP/2020/134). P-A.R. and M.M.M. acknowledged the financial support from the Netherlands Enterprise Agency under contract SOL18001 of the SOLAR ERA NET CUSTCO project.

Conflict of Interest

The authors declare no conflict of interest.

Data Availability Statement

The data that support the findings of this study are available from the corresponding author upon reasonable request.

Keywords

pulsed laser deposition, indium tin oxide, perovskite solar cells, optoelectronic devices

Received: January 7, 2022
Revised: April 1, 2022
Published online:

[1] M. Morales-Masis, S. De Wolf, R. Woods-Robinson, J. W. Ager, C. Ballif, *Adv. Electron. Mater.* **2017**, *3*, 1600529.
[2] Y. Smirnov, L. Schmengler, R. Kuik, P. Repecaud, M. Najafi, D. Zhang, M. Theelen, E. Aydin, S. Veenstra, S. De Wolf, M. Morales-Masis, *Adv. Mater. Technol.* **2021**, *6*, 2000856.
[3] J. B. Franklin, J. B. Gilchrist, J. M. Downing, K. A. Roy, M. A. McLachlan, *J. Mater. Chem. C* **2014**, *2*, 84.
[4] R. A. Afre, N. Sharma, M. Sharon, M. Sharon, *Rev. Adv. Mater. Sci.* **2018**, *53*, 79.
[5] P. K. Nayak, S. Mahesh, H. J. Snaith, D. Cahen, *Nat. Rev. Mater.* **2019**, *4*, 269.
[6] M.-H. Chang, D. Das, P. V. V Varde, M. Pecht, *Microelectron. Reliab.* **2012**, *52*, 762.
[7] Y. Yin, M. U. Ali, W. Xie, H. Yang, H. Meng, *Mater. Chem. Front.* **2019**, *3*, 970.
[8] C.-C. Wu, *RSC Adv.* **2018**, *8*, 11862.
[9] P. Spinelli, R. Fuentes Pineda, M. Scigaj, T. Ahmad, K. Wojciechowski, *Appl. Phys. Lett.* **2021**, *118*, 241110.
[10] V. Adinolfi, E. H. Sargent, *Nature* **2017**, *542*, 324.
[11] W. Yu, F. Li, L. Yu, M. R. Niazi, Y. Zou, D. Corzo, A. Basu, C. Ma, S. Dey, M. L. Tietze, U. Buttner, X. Wang, Z. Wang, M. N. Hedhili, C. Guo, T. Wu, A. Amassian, *Nat. Commun.* **2018**, *9*, 5354.
[12] J. Yan, A. Rath, H. Wang, Z. Q. C. Ng, S. J. Pennycook, D. H. C. Chua, *J. Phys. Chem. C* **2021**, *125*, 11115.
[13] H. Wang, S. Li, X. Liu, Z. Shi, X. Fang, J. He, *Adv. Mater.* **2021**, *33*, 2003309.
[14] B. Lüssem, A. Günther, A. Fischer, D. Kasemann, K. Leo, *J. Phys.: Condens. Matter* **2015**, *27*, 443003.
[15] J. Ávila, C. Momblona, P. P. Boix, M. Sessolo, H. J. Bolink, *Joule* **2017**, *1*, 431.
[16] D. Pérez-Del-Rey, L. Gil-Escrig, K. P. S. Zanoni, C. Dreessen, M. Sessolo, P. P. Boix, H. J. Bolink, *Chem. Mater.* **2019**, 31.
[17] E. Aydin, C. Altinkaya, Y. Smirnov, M. A. Yaqin, K. P. S. Zanoni, A. Paliwal, Y. Firdaus, T. G. Allen, T. D. Anthopoulos, H. J. Bolink, M. Morales-Masis, S. De Wolf, *Matter* **2021**, *4*, 3549.
[18] H. Kanda, A. Uzum, A. K. Baranwal, T. A. N. Peiris, T. Umeyama, H. Imahori, H. Segawa, T. Miyasaka, S. Ito, *J. Phys. Chem. C* **2016**, *120*, 28441.
[19] Q. H. Fan, M. Deng, X. Liao, X. Deng, *J. Appl. Phys.* **2009**, *105*, 033304.
[20] H. Lei, K. Ichikawa, Y. Hoshi, M. Wang, T. Uchida, Y. Sawada, *Thin Solid Films* **2010**, *518*, 2926.
[21] D. Hamaguchi, S. Kobayashi, T. Uchida, Y. Sawada, H. Lei, Y. Hoshi, *Jpn. J. Appl. Phys.* **2016**, *55*, 106501.
[22] A. J. Bett, K. M. Winkler, M. Bivour, L. Cojocaru, Ö. Ş. Kabakli, P. S. C. Schulze, G. Siefer, L. Tutsch, M. Hermle, S. W. Glunz, J. C. Goldschmidt, *ACS Appl. Mater. Interfaces* **2019**, *11*, 45796.
[23] H. Lei, K. Ichikawa, Y. Hoshi, M. Wang, Y. Sawada, T. Uchida, *Trans. Mater. Res. Soc. Jpn.* **2009**, *34*, 321.
[24] D. Depla, G. Buyle, J. Haemers, R. De Gryse, *Surf. Coat. Technol.* **2006**, *200*, 4329.
[25] E. Terzini, G. Nobile, S. Loreti, C. Minarini, T. Polichetti, P. Thilakan, *Jpn. J. Appl. Phys.* **1999**, *38*, 3448.
[26] F. J. Ramos, S. Jutteau, J. Posada, A. Bercegol, A. Rebai, T. Guillemot, R. Bodeux, N. Schneider, N. Loones, D. Ory, C. Broussillou, G. Goaer, L. Lombez, J. Rousset, *Sci. Rep.* **2018**, *8*, 16139.
[27] M. Jaysankar, W. Qiu, M. van Eerden, T. Aernouts, R. Gehlhaar, M. Debucquoy, U. W. Paetzold, J. Poortmans, *Adv. Energy Mater.* **2017**, *7*, 1602807.
[28] H. A. Dewi, H. Wang, J. Li, M. Thway, R. Sridharan, R. Stangl, F. Lin, A. G. Aberle, N. Mathews, A. Bruno, S. Mhaisalkar, *ACS Appl. Mater. Interfaces* **2019**, *11*, 34178.
[29] T. Wahl, J. Hanisch, S. Meier, M. Schultes, E. Ahlswede, *Org. Electron.* **2018**, *54*, 48.
[30] T. Soto-Montero, W. Soltanpoor, M. Morales-Masis, *APL Mater.* **2020**, *8*, 110903.
[31] A. Ojeda-G-P, M. Döbeli, T. Lippert, *Adv. Mater. Interfaces* **2018**, *5*, 1701062.
[32] K. Matsubara, P. Fons, K. Iwata, A. Yamada, K. Sakurai, H. Tampo, S. Niki, *Thin Solid Films* **2003**, *431–432*, 369.
[33] S. Schubert, F. Schmidt, H. von Wenckstern, M. Grundmann, K. Leo, L. Müller-Meskamp, *Adv. Funct. Mater.* **2015**, *25*, 4321.
[34] Y. Smirnov, P.-A. Repecaud, L. Tutsch, I. Florea, K. P. S. Zanoni, A. Paliwal, H. J. Bolink, P. R. i Cabarrocas, M. Bivour, M. Morales-Masis, *Mater. Adv.* **2022**, *3*, 3469.
[35] E. Aydin, M. De Bastiani, X. Yang, M. Sajjad, F. Aljamaan, Y. Smirnov, M. N. Hedhili, W. Liu, T. G. Allen, L. Xu, E. Van Kerschaver, M. Morales-Masis, U. Schwingenschlögl, S. De Wolf, *Adv. Funct. Mater.* **2019**, *29*, 1901741.
[36] J. B. Franklin, J. M. Downing, F. Giuliani, M. P. Ryan, M. A. McLachlan, *Adv. Energy Mater.* **2012**, *2*, 528.
[37] S. Wang, W. Li, M. Morbidoni, M. A. McLachlan, J. Zhang, *Appl. Nanosci.* **2020**, *10*, 1871.
[38] J. H. Park, J. Seo, S. Park, S. S. Shin, Y. C. Kim, N. J. Jeon, H.-W. Shin, T. K. Ahn, J. H. Noh, S. C. Yoon, C. S. Hwang, S. Il Seok, *Adv. Mater.* **2015**, *27*, 4013.
[39] N. Rodkey, S. Kaal, P. Sebastia-Luna, Y. A. Birkhölzer, M. Ledinsky, F. Palazon, H. J. Bolink, M. Morales-Masis, *Chem. Mater.* **2021**, *33*, 7417.
[40] E. Holmelund, B. Thestrup, J. Schou, N. B. Larsen, M. M. Nielsen, E. Johnson, S. Tougaard, *Appl. Phys. A: Mater. Sci. Process.* **2002**, *74*, 147.
[41] H. Kim, A. Piqué, J. S. Horwitz, H. Mattoussi, H. Murata, Z. H. Kafafi, D. B. Chrisey, *Appl. Phys. Lett.* **1999**, *74*, 3444.
[42] C. Viespe, C. Grigoriu, M. Popescu, F. Sava, A. Lörinczi, A. Velea, S. Zamfira, J. Optoelectron, *Adv. Mater.* **2007**, *9*, 3563.
[43] T. K. Yong, S. S. Yap, G. Sáfrán, T. Y. Tou, *Appl. Surf. Sci.* **2007**, *253*, 4955.
[44] H. Kim, C. M. Gilmore, A. Piqué, J. S. Horwitz, H. Mattoussi, H. Murata, Z. H. Kafafi, D. B. Chrisey, *J. Appl. Phys.* **1999**, *86*, 6451.
[45] S. H. Kim, N.-M. Park, T. Kim, G. Sung, *Thin Solid Films* **2005**, *475*, 262.
[46] C. Viespe, I. Nicolae, C. Sima, C. Grigoriu, R. Medianu, *Thin Solid Films* **2007**, *515*, 8771.
[47] J. B. Choi, J. H. Kim, K. A. Jeon, S. Y. Lee, *Mater. Sci. Eng.: B* **2003**, *102*, 376.
[48] M. Socol, N. Preda, O. Rasoga, A. Costas, A. Stanculescu, C. Breazu, F. Gherendi, G. Socol, *Coatings* **2018**, *9*, 19.

[49] M.-S. Kim, B.-G. Kim, J. Kim, *ACS Appl. Mater. Interfaces* **2009**, *1*, 1264.
[50] M. A. Green, *Appl. Phys. Lett.* **2016**, *108*, 081111.
[51] M. De Bastiani, G. Armaroli, R. Jalmood, L. Ferlauto, X. Li, R. Tao, G. T. Harrison, M. K. Eswaran, R. Azmi, M. Babics, A. S. Subbiah, E. Aydin, T. G. Allen, C. Combe, T. Cramer, D. Baran, U. Schwingenschlögl, G. Lubineau, D. Cavalcoli, S. De Wolf, *ACS Energy Lett.* **2022**, *7*, 827.
[52] J. I. Goldstein, D. E. Newbury, J. R. Michael, N. W. M. Ritchie, J. H. J. Scott, D. C. Joy, *Scanning Electron Microscopy and X-ray Microanalysis*, Fourth Edi., Springer, **2018**.
[53] I. C. Kaya, K. P. S. Zanoni, F. Palazon, M. Sessolo, H. Akyildiz, S. Sonmezoglu, H. J. Bolink, *Adv. Energy Sustainability Res.* **2021**, *2*, 2000065.
[54] Available in "www.nrel.gov/pv/text-spectral-mismatch-corrections.html" (accessed: March 2022).